


# TOWARDS THE INTEGRATION OF NEUROPHYSIOLOGICAL SIGNALS AND HUMAN BODY DYNAMICS FOR ADAPTIVE CONTROL ALLOCATION

Tobias Treichl[1,2] & Tanya S. Paul[3]

[1]Institute of Flight Systems, German Aerospace Center (DLR), Munich, Germany
[2]Neuromuscular Diagnostics, TUM School of Medicine and Health, Technical University Munich (TUM), Germany
[3]Thales cortAIx, Palaiseau, France

## Abstract

The accelerating integration of autonomous systems in aviation is transforming command and control paradigms, requiring effective human-AI collaboration that considers both cognitive and biodynamic states of operators. This research explores the impact of operating in dynamic environments on task performance and neurophysiological measurements, and examines whether integrating biodynamic feedthrough features into pilot state models can enhance prediction accuracy.

A single-subject study using a motion simulator and the Multi-Attribute Task Battery - II was conducted to assess the effects of motion conditions on a fine motor task and neurophysiological signals. The study focused on two hypotheses: that pilot performance differs between no-acceleration and acceleration conditions, and that neurophysiological signals correlate with body dynamics under varying accelerations.

Results demonstrated consistent impact of turbulence and workload on task performance and joystick input within the subject. Turbulence also influenced neurophysiological signals like EEG and cardiorespiration. Integrating knowledge of biomechanics and task dynamics provides a promising indication that prediction accuracy can be improved, by using a biodynamic feedthrough simulation model. However, further studies are needed to conclusively demonstrate enhancements in prediction accuracy. These findings highlight the importance of integrated models that account for both physical and cognitive factors to enhance human-AI collaboration in aviation.

**Keywords:** Adaptive control allocation, human state modeling, biodynamic modeling

| Symbol | Description |
|---|---|
| **Environment** | |
| $\mathbf{r}$ | Cursor reference position |
| $\mathbf{y}$ | cursor position |
| $\hat{\mathbf{y}}$ | Sensory feedback of cursor position |
| $\delta_{ref}$ | Joystick reference position |
| $\delta_{act}$ | Joystick position |
| $\mathbf{r}_{sim}$ | Simulator cockpit position |
| $\varphi, \theta, \psi$ | Simulator cockpit Euler angles |
| $\omega_{sim}$ | Simulator cockpit angular rates |
| $f$ | Cut-off frequency of critical damping filter |
| $\sigma_n$ | Normal noise standard deviation |
| $\Delta t_n$ | Normal noise sampling time |
| $k_j$ | Gain of joystick input |
| $k^c$ | Proportional gain of tracking controller |
| $T_i^c$ | Time constant of integrator block of tracking controller |
| $T_i^d$ | Time constant of derivative block of tracking controller |
| **Human Body Model** | |
| $\mathbf{k}_e$ | Arm endpoint stiffness in forward, sideward and upward directions |
| $\lambda_e$ | Damping ratio at arm endpoint |
| $\tau_d^e$ | Feedback delay of arm |
| $\mathbf{k}_t$ | Stiffness of torso joints |
| $\lambda_t$ | Damping ratio of torso joints |
| $\tau_d^t$ | Feedback delay of torso |
| $\mathbf{r}_{ref}^h$ | Reference position of the human models hand |
| $\mathbf{r}_{act}^h$ | Position of the human models hand |
| $\mathbf{T}_{ref}^h$ | Reference orientation matrix of the hand |
| $\mathbf{T}_{act}^h$ | Orientation matrix of the hand |
| $\mathbf{f}_{exp}^h$ | Expected force at the hand |
| **Optimization Problem** | |
| $J$ | Cost function |
| $e$ | Root mean squared error of cursor (forward or sideward) |
| $\hat{}$ | Normalized difference of quantity between experiment and simulation |
| $P$ | Power of a signal |
| $a$ | Mean squared acceleration of a signal |
| $f_{ch}$ | Direction change frequency of a signal |

Table 1 – Symbols used in this work

## 1. Introduction

The accelerating integration of autonomous systems and artificial intelligence (AI) into contemporary flight operations is fundamentally reshaping collaborative command and control (C2) paradigms across the aerospace domain. As aircraft operations become increasingly complex and dynamic, the

challenge of effective human-AI teaming transcends traditional technical interoperability, demanding a nuanced approach that holistically accounts for both cognitive and biodynamic states of the human operator. This research seeks to advance a comprehensive and adaptive model for control allocation between human pilots and autonomous systems, called *Sharing Tasks with Autonomous Resources* (STAR) [2] thereby enhancing mission effectiveness, situational awareness, and decision-making agility for both aircrew and commanders. The presented work aligns well with the framework of Observability, Predictability and Directability (OPD) [3], which aims to support seamless integration and effective collaboration between humans and autonomous agents.

While significant progress has been made in modeling operator state, prior research in human-machine teaming has tended to focus on isolated domains — often emphasizing neurophysiological indicators such as mental workload (hereinafter referred to simply as workload) and fatigue [4] [5]. Although informative, these approaches inadequately address the interplay between cognitive and physical stresses encountered in highly dynamic flight scenarios, where rapid adaptation and seamless control transitions are imperative. This is suggested by previous work, which has already indicated a correlation between physical stresses and workload in treadmill experiments [7].

A critical gap persists: The joint consideration of both neurophysiological parameters and biodynamic feedthrough (BDFT), in a high fidelity simulation environment, emulating real aircraft movements. Thereby, BDFT describes the unintended transmission of forces or motion through the human body onto a control task. The findings of this study suggest that a fusion of these metrics is essential to accurately anticipate pilots performance limitations and inform intelligent, context-sensitive allocation of control between human and AI agents. In this work, a pilot study with one participant was conducted to investigate the effect of simulator movement, particularly different turbulence levels, on task performance and on neurophysiological signals, using the NASA Multi-Attribute Task Battery - II (MATB). It should be emphasized that the present study was conducted as a proof-of-concept pilot experiment involving a single participant. The primary objective was not to establish statistically generalizable physiological effects, but rather to evaluate the feasibility of simultaneously acquiring neurophysiological, cardio-respiratory, and biodynamic measurements during turbulence-induced simulator motion. Consequently, the reported findings should be interpreted as preliminary observations intended to inform the design of future multi-participant studies.

## 2. Methods

### 2.1 Hypotheses

Two hypotheses have been formulated to investigate the potential of integrating neurophysiological signals and BDFT in order to better the STAR adaptive control allocation model's performance and anticipation capabilities. These are:

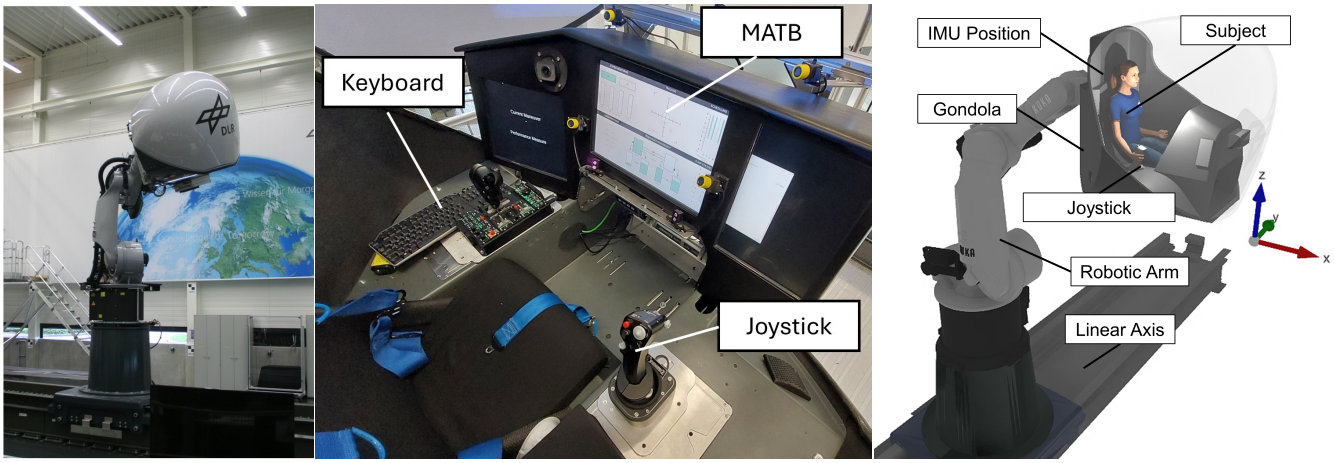
- **Performance Difference Hypothesis:** There will be a decrease in pilot performance metrics with increasing turbulence levels during task execution.
- **Neurophysiological Correlation Hypothesis:** Neurophysiological signal activity such as electroencephalography (EEG), and heart rate will exhibit associations with varying turbulence conditions.

### 2.2 Experimental Setup

The experimental setup consists of a robotic motion simulator located at the DLR Dynamic Motion Simulation Center, in which the MATB is performed.

#### *2.2.1 Motion Simulation*

The acceleration stimuli representing level flight under different turbulence conditions are produced using the robotic motion simulator shown in Fig. 1a. Realistic aircraft accelerations are computed using a modified flight model of a DA42 aircraft, which was validated on the motion simulator by military pilots in a previous study [13]. To generate motions corresponding to turbulent level flight, air-velocity components computed using a Dryden turbulence model [17] are applied to the flight model. For the simulation of light turbulence, a probability of exceedance (PoE) of $10^{-2}$ is used, whereas




(a) (b) (c)

Figure 1 – Experimental setup. (a) Robotic Motion Simulator reproducing aircraft accelerations. (b) View inside the motion simulator gondola with MATB-II running on the center screen. A keyboard and the joystick on the right are used for MATB-II inputs. (c) Visualization of the human body model inside the motion simulator. The model is used to estimate the biodynamic feedtrough on the tracking task.

severe turbulence is represented by a PoE of $10^{-4}$. Via the PoE the amplitude of turbulence can be modulated.

The transfer of aircraft accelerations to the robot workspace is performed using a classical washout filter and a damped least-squares inverse kinematics approach from [14]. It should be noted that, due to washout filtering and the dynamic limits of the motion system, the accelerations experienced inside the cockpit are usually lower than those predicted by the aircraft model. With the presented motion simulation setup, the resulting acceleration signal power in the forward direction was $0.15\ \frac{m^2}{s^4}$ for light turbulence and $0.45\ \frac{m^2}{s^4}$ for severe turbulence. In the sideward direction, the corresponding values were $0.06\ \frac{m^2}{s^4}$ and $0.08\ \frac{m^2}{s^4}$, respectively.

### *2.2.2 Workload Manipulation*

During the experiment, the participant is seated inside the gondola (see Fig. 1b). The participant operates the two-axis joystick with the right hand (dominant hand). A keyboard attached to the participant's thighs using Velcro straps is operated with the left hand. MATB is displayed on the center screen directly in front of the participant (see Fig. 1b). The MATB consists of four standardized tasks that can be parameterized individually to generate desired workload levels [18].

Three MATB configurations were used throughout the experiment: a tracking-only (TR) condition, a low-workload (LWL) condition, and a high-workload (HWL) condition. The workload conditions include the systems monitoring, resource management, and tracking subtasks [18]. The low- and high-workload conditions differ in the event frequency of the systems monitoring and resource management tasks. The workload configurations are based on the study presented in [7], with the communications task replaced by the tracking task.

Particular attention is given to the tracking task, since it is expected to be the MATB subtask most affected by accelerations acting on the human body. Additionally, unlike the other subtasks, the control input is measured continuously, providing granular insight into human body dynamics and the associated BDFT effects on tracking performance. The MATB tracking task requires continuous compensatory control to keep a cursor, which is displaced by a predefined force function, close to the target reticle [18]. The joystick sensitivity can be adjusted via the gain parameter $k_j$. In this work, the gain was increased to $k_j = 4$ compared to the default value of $k_j = 1$ in order to create a more demanding fine-motor control task. The objective was to keep the cursor as close as possible to the reticle.

Subjective ratings of workload and motion sickness were collected using the NASA Task Load Index

(TLX) and the Simulator Sickness Questionnaire (SSQ) [19, 20]. The OpenMATB project was used for the implementation of the MATB tasks [12].

## 2.3 Experimental Design

### *2.3.1 Preparation of the Subject*

The experimental protocol was approved by the DLR ethics committee. The participant was fully informed about the purpose and procedure of the study and provided informed consent. The participant was given the opportunity to ask questions at any time and was informed about the possibility of withdrawing from the experiment without consequences.
Next, the sensors were applied to the participant. The ANT Neuro EEG headset was positioned. The participant then put on the Hexoskin shirt and smartwatch. Subsequently, the participant was seated inside the gondola and secured using a five-point harness, and the EEG headset was connected to the amplifier. Finally, the keyboard was attached to the participant's thighs using Velcro straps. All sensors were operated according to the manufacturer's specifications

### *2.3.2 Experiment*

The experiment began with a five-minute baseline measurement of the neurophysiological signals. During this period, the participant remained seated inside the stationary gondola and did not perform any task. We used the test matrix shown in Fig. 2 to define the remaining experimental trials.

| | **No turbulence (No)** | **Low turbulence (Lo)** | **High turbulence (Hi)** |
|---|---|---|---|
| **MATB-II tracking only (TR)** | 2 min | 2 min | 2 min |
| **MATB-II low workload (LWL)** | 5 min | 5 min | 5 min |
| **MATB-II high workload (HWL)** | 5 min | 5 min | 5 min |

Figure 2 – Test matrix used in the experiment. Three MATB workload conditions and three turbulence conditions were combined, resulting in nine experimental trials.

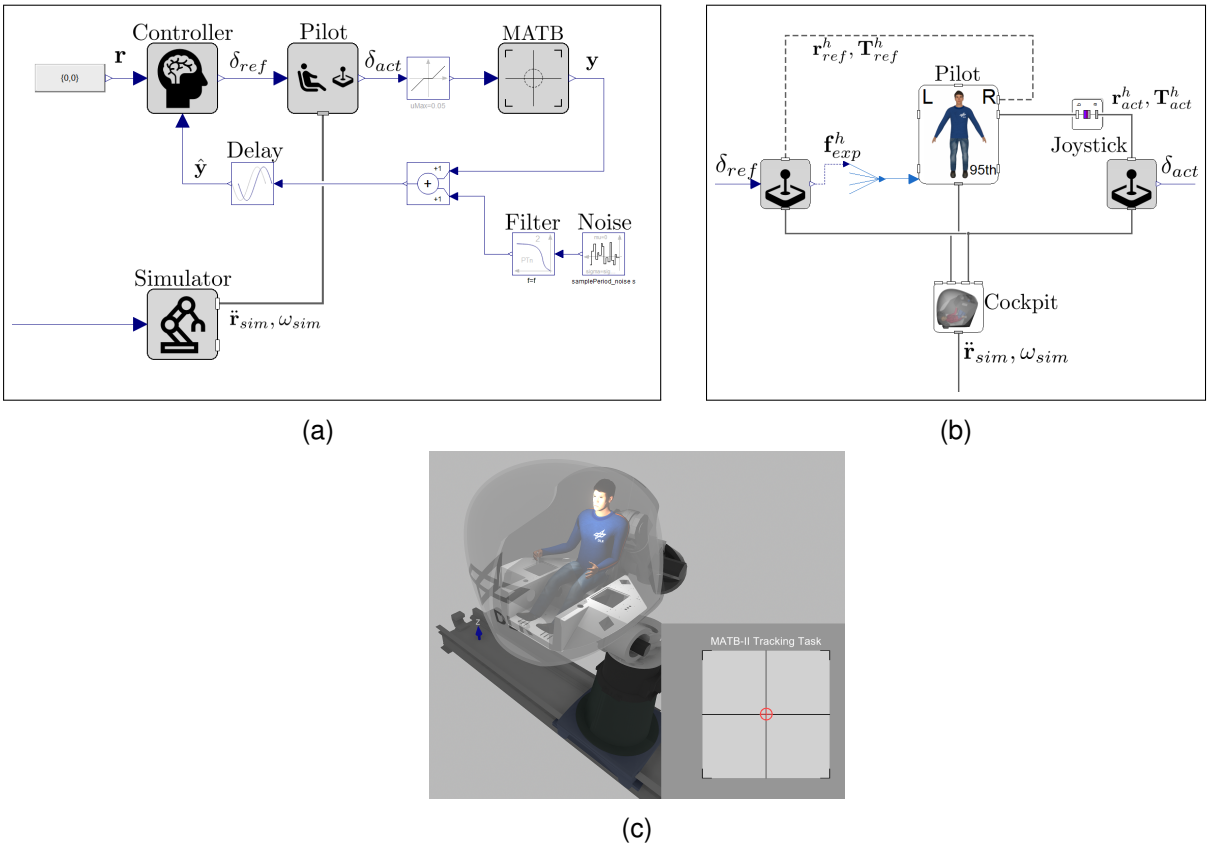
The tracking-only, low-workload, and high-workload conditions represent the workload manipulations described in Section 2.2.2. The no-turbulence (No), low-turbulence (Lo), and high-turbulence (Hi) conditions represent the physical motion stimuli. Combining both factors results in a total of nine experimental conditions. The workload conditions lasted five minutes each. The tracking-only conditions lasted two minutes. The order of the experimental trials went from tracking only to high workload, starting with the no turbulence condition. Before each trial, the motion corresponding to the selected turbulence condition was started. The participant independently determined the onset of the MATB-II task. Following the baseline measurement and after each experimental condition, the participant completed the SSQ and TLX questionnaires.

## 2.4 Data Collection

To investigate the relationship between mental state and physical human-machine interaction, a multimodal data collection framework integrating biomechanical and neurophysiological measurements was implemented. The neurophysiological data comprised cardiopulmonary measures (heart rate, heart rate variability, and respiratory rate) as well as EEG. Accelerations acting on the participant were measured using a Litef $\mu$IMU at 100 Hz, while joystick inputs were recorded at 200 Hz. These signals constitute the biomechanical data stream. The results of the MATB tasks were recorded using the built-in logging functionality of OpenMATB [12]. The log files contain, among other information, timestamps of task events, joystick inputs, and cursor positions. Results of the subjective questionnaires were also stored together with the OpenMATB log files.

## 2.5 Simulation of Biodynamic Feedthrough on MATB Tracking Task

The Modelica modeling language, specifically the DLR Robots [8] and HumanBody Library [11] were used to model the BDFT on the MATB tracking task. The benefit of the BDFT simulation is the ability to estimate additional quantities like error in motor control or the expected decrease of task performance induced by aircraft motion, which cannot be measured directly.




(a) (b)

(c)

Figure 3 – (a) Overall BDFT simulation model, consisting of a tracking controller, a pilot, the MATB tracking task and a simulated robot. The simulated pilot is controlling the cursor position in the loop under disturbance of movement. (b) Biodynamic model of the pilot interacting with the joystick. (c) Visualization of the simulated MATB tracking task performed by biodynamic pilot model, perturbed by the simulated motion simulator. In the lower right corner the cursor and reticle are shown.

### *2.5.1 Overall Model*

Figure 3a shows the top-level architecture of the BDFT simulation model. A cascaded control approach was employed. The outer control loop shown in the figure represents the visual feedback during the tracking task. The cursor reference position $\mathbf{r}$ is fixed at zero and compared with the sensory feedback $\hat{\mathbf{y}}$. Based on this error, the tracking controller generates the reference joystick position $\delta_{ref}$.

Sensory feedback is modeled by adding normally distributed noise with standard deviation $\sigma_n$ and sampling interval $\Delta t_n$ to the cursor position $\mathbf{y}$ in both directions. The resulting signal is filtered using a second-order critically damped filter with cut-off frequency $f$. This approach is intended to approximate perceptual uncertainty and neural processing delays while producing smooth controller inputs. The filtered feedback resulted in realistic control behavior in comparison to the experimental observations (see section 3.1).

The reference joystick trajectory $\delta_{ref}$ is passed to the pilot model described in Section 2.5.3. The pilot model follows this trajectory while accounting for the relevant effects of motor control, body dynamics, and acceleration-induced perturbations (see section 2.5.3). Simulator motion is transferred to the pilot via a Modelica multi-body frame connection including cockpit position $\mathbf{r}_{sim}$, and orientation $\phi, \theta, \psi$ as

well as the accelerations $\ddot{\mathbf{r}}_{sim}$ and angular rates $\omega_{sim}$ (see section 2.5.5). Consequently, cockpit motion directly excites the biodynamic response of the pilot.
The resulting joystick position $\delta_{act}$ is filtered by a dead zone of $0.05\%$ to match the experimental setup before being passed to the MATB tracking task model, which computes the resulting cursor position $\mathbf{y}$.

### 2.5.2 Tracking Controller

The tracking controller transforms the perceived cursor position $\hat{\mathbf{y}}$ into the joystick reference trajectory $\delta_{ref}$. A PID controller was selected as a simple approximation of the pilot's visual tracking strategy.
The controller parameters $k^c$, $T_i^c$, and $T_i^d$ correspond to the proportional gain, integral time constant, and derivative time constant, respectively. Rather than representing physiological control mechanisms directly, these parameters provide sufficient flexibility to reproduce the observed tracking behavior in the absence of BDFT and were therefore included in the parameter optimization described in Section 2.5.6.

### 2.5.3 Pilot Model

Figure 3b shows the modeling of the pilot interacting with the joystick. The joystick handle is modelled as a rigid mass of $0.5\,\mathrm{kg}$, the center of mass is located at half of the distance between the rotation axes and the grip point of the hand. The grip point is located at a distance of $13\,\mathrm{cm}$ from the pivot point of the stick. The joystick has two degrees of freedom, one in the forward / backward and one in sideward direction. Resistance of the joystick axes is modelled as a spring damper system with a stiffness of $1.7\,\mathrm{N\,m\,rad^{-1}}$ and damping constant of $0.085\,\mathrm{N\,m\,s\,rad^{-1}}$. The choosen parameters resulted in similar oscillation behavior compared to the real setup. The pilot model was modelled using a mass of $95\,\mathrm{kg}$ and the $95^{th}$ percentile parameter set for body height, resembling the anthropometric characteristics of the subject .
The general control structure is based on the approach presented in [10] and briefly described below. Human motor control is assumed to rely on internal models of both the body and the environment. To account for this behavior, two joystick models are used in the simulation.
The first joystick model represents the pilot's internal model of the environment. It is used to determine the desired hand position $\mathbf{r}_{ref}^h$, hand orientation $\mathbf{T}_{ref}^h$, and expected interaction forces $\mathbf{f}_{exp}^h$ required to achieve the reference joystick trajectory $\delta_{ref}$. The second joystick model represents the physical joystick that is mechanically coupled to the human model and the simulator environment.
For simulation of the pilots biodynamics the DLR HumanBody Library was used. The library is designed for the simulation of physical human machine interaction, thereby considering the most relevant effects of human biomechanics and motor control, which are covered in this work only with a high level view. For more detail please refer to the given references:

- **Multi-body representation:** The human body is represented as a rigid-body system with 14 joints and 33 degrees of freedom. Muscle effects are approximated through joint torques, providing computational efficiency while retaining the dominant biomechanical dynamics [11, 9].
- **Inverse kinematics:** Desired hand poses are specified in Cartesian space and converted into joint configurations using inverse kinematics. Redundant degrees of freedom are used to avoid singularities and generate natural arm postures [11].
- **Internal models:** The control architecture includes feedforward inverse dynamics and delayed feedback pathways inspired by human motor control. This allows compensation of expected interaction forces and external disturbances [10].
- **Joint impedance:** Neuromuscular stiffness and reflex-like behavior are represented by Cartesian impedance control at the arm endpoint, enabling realistic interaction with the environment [9].

### 2.5.4 MATB Tracking Task Simulation Model

The MATB block is a Modelica implementation of the tracking task based on the OpenMATB project [12]. Aligning with the experimental setup from section 2.2.2, the joystick gain was increased to $k_j = 4$, in order to simulate a fine motor task.

### 2.5.5 Motion Simulator Model

The motion simulator is represented using the measured IMU data rather than commanded robot trajectories. This approach captures structural dynamics and vibration modes of the robot that are not represented by a rigid-body model alone. Measured linear accelerations $\ddot{\mathbf{r}}_{sim}$ and angular rates $\omega_{sim}$ are therefore applied directly to the simulation. Cockpit position and orientation are reconstructed from the commanded robot trajectory only for visualization purposes, like in fig. 3c.

### 2.5.6 Parameter Optimization

The simulation model described in Section 2.5.1 was exported as a Functional Mock-up Unit (FMU) to enable execution within a Python environment [21]. For parameter optimization, the model outputs the simulated cursor position $\mathbf{y}$ and joystick position $\delta_{act}$. Both signals are filtered using a moving-average filter with a window length of $0.5\,\mathrm{s}$. The moving-average filtering prevents high-frequency oscillations from being artificially rewarded during optimization.
Due to the stochastic nature of the tracking task, a direct point-wise comparison between simulated and experimental trajectories is not sufficient. Instead, several signal characteristics describing the similarity of tracking performance and control behavior are evaluated and combined into a cost function.

$$\hat{e}_f = \frac{e_f^{exp} - e_f^{sim}}{e_f^{exp}} \tag{1}$$

$$\hat{e} = \hat{e}_f^2 + \hat{e}_s^2 \tag{2}$$

$$J_{condition} = 2\hat{e}_{cur} + \hat{P}_{cur} + \hat{a}_{cur} + \hat{f_{ch}}_{cur} + \hat{a}_{stick} \tag{3}$$

$$J = 2J_{Hi} + 2J_{Lo} + J_{No} \tag{4}$$

Equations 1–4 define the optimization cost function. Equation 1 computes the normalized difference between the simulated and experimentally measured RMS tracking error in one direction, while Equation 2 combines the forward and sideward components into a single RMS error term.
To account for similarities beyond overall tracking accuracy, additional signal characteristics are included in Equation 3: signal power $P$, mean squared acceleration $a$, and direction change frequency $f_{ch}$. The first four terms are derived from the cursor position signal $\mathbf{y}$, whereas $\hat{a}_{stick}$ is computed from the joystick signal $\delta_{act}$. Equation 4 combines the costs of all turbulence conditions, with increased weighting of the low- and high-turbulence conditions, as these are most relevant for identifying biodynamic feedthrough effects.
The tracking controller parameters $k^c$, $T_i^d$, $T_i^c$, $\sigma_n$, $\Delta t_n$, and $f$ were selected as optimization variables. In addition, the biodynamic parameters $\mathbf{k}_e$, $\lambda_e$, $\tau_d^e$, $\mathbf{k}_t$, $\lambda_t$, and $\tau_d^t$ were optimized. Parameter estimation was performed using the Optuna framework with a Tree-structured Parzen Estimator (TPE) sampler.

## 2.6 Neurophysiological Signals

### 2.6.1 EEG

In this study, EEG signals were first imported from a time-stamped experimental recording and organized according to task conditions representing different workload and turbulence levels. Each EEG channel was preprocessed using a standard signal cleaning pipeline, including mean removal, 50 Hz notch filtering to suppress power-line noise, and a 1–40 Hz Butterworth bandpass filter to retain physiologically relevant neural activity while removing slow drifts and high-frequency artifacts. The cleaned signals were then segmented by experimental condition, and spectral features were extracted using Welch's method to estimate the Power Spectral Density (PSD) for each EEG channel. Band-specific neural activity was quantified by integrating the PSD within canonical frequency ranges

— delta (1–4 Hz), theta (4–8 Hz), alpha (8–13 Hz), and beta (13–30 Hz) — using numerical integration (trapezoidal rule), resulting in a high-dimensional feature set representing spatial (channel-wise) and spectral brain activity. These features were aggregated in a structured dataset and subsequently used to derive condition-level neurophysiological markers. Specifically, band-power values were averaged across channels to obtain global spectral indicators per condition, from which a primary EEG-derived workload metric was constructed following established neuroergonomic approaches [15, 6]. The workload Index was defined as $(\theta + \beta)/\alpha$, where theta ($\theta$) activity is commonly associated with increased cognitive control and working memory engagement, alpha ($\alpha$) activity is typically linked to cortical idling and relaxed states, and beta ($\beta$) activity reflects active information processing and attentional demand.
These indices were then normalized with respect to a baseline condition and statistically compared across experimental scenarios (e.g. workload and turbulence levels), enabling visualization of how cognitive load varies under different operational demands. The resulting analysis pipeline therefore transforms raw EEG time-series data into interpretable workload-related biomarkers, supporting condition discrimination and providing a step torwards quantitative evidence of mental effort modulation across tasks.

### *2.6.2 Cardio-Respiratory Dynamics*

Neurophysiological measurements were acquired to characterize the participant's cognitive and physiological state throughout the experiment [1]. Cardiovascular activity was monitored using a multimodal sensing approach combining a Hexoskin smart shirt and a smartwatch. Heart rate estimates from both devices were integrated to generate a fused heart rate measure expressed in beats per minute (BPM), providing a robust representation of cardiac activity.
R–R interval data acquired from the Hexoskin system were processed through the SensorHub framework, which performed signal conditioning and artifact filtering prior to feature extraction. These filtered inter-beat intervals were subsequently used to compute a range of heart rate variability (HRV) metrics. Frequency-domain HRV features were calculated using both short-term (120 s) and long-term (300 s) analysis windows to capture autonomic dynamics across multiple timescales. The extracted spectral features included High-Frequency (HF), Low-Frequency (LF), Very-Low-Frequency (VLF), and Ultra-Low-Frequency (ULF) power components.

## 3. Results

### 3.1 MATB-II Tracking Task

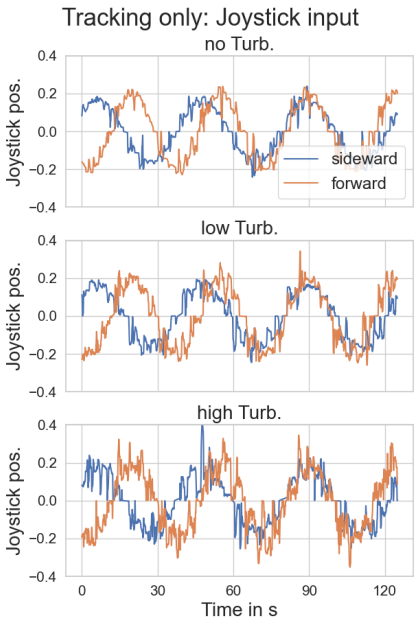



Figure 4 – Joystick input in tracking only condition for different turbulence levels. Variability at the joystick increased with simulator motion.

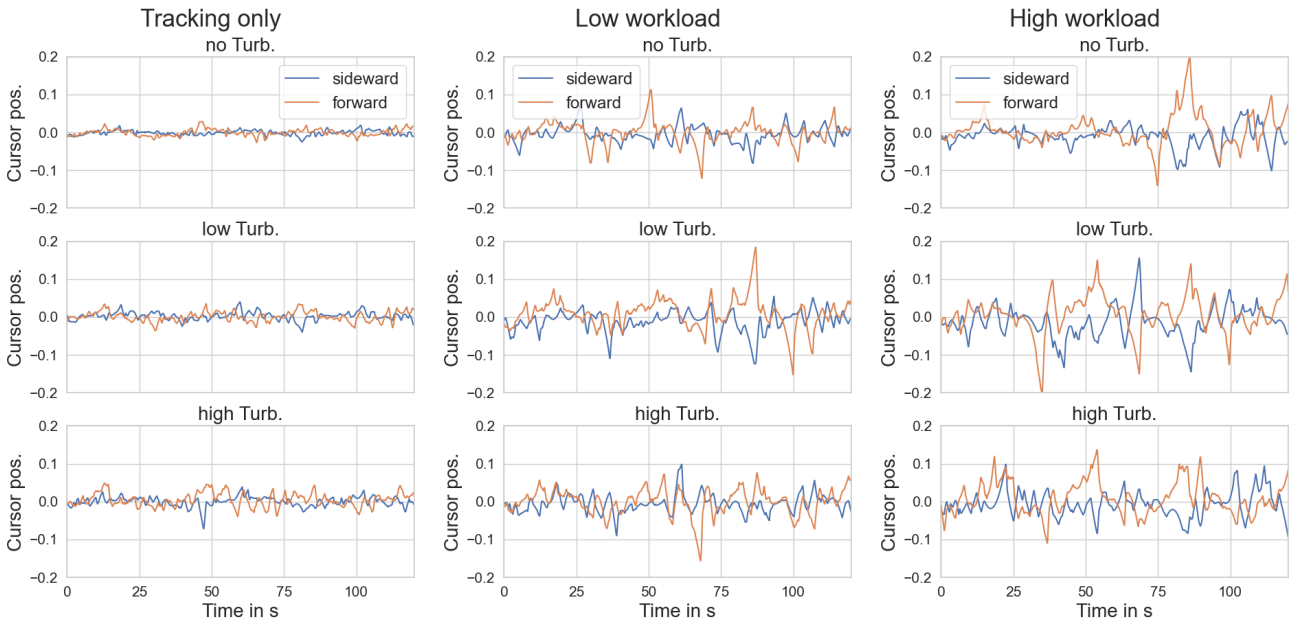
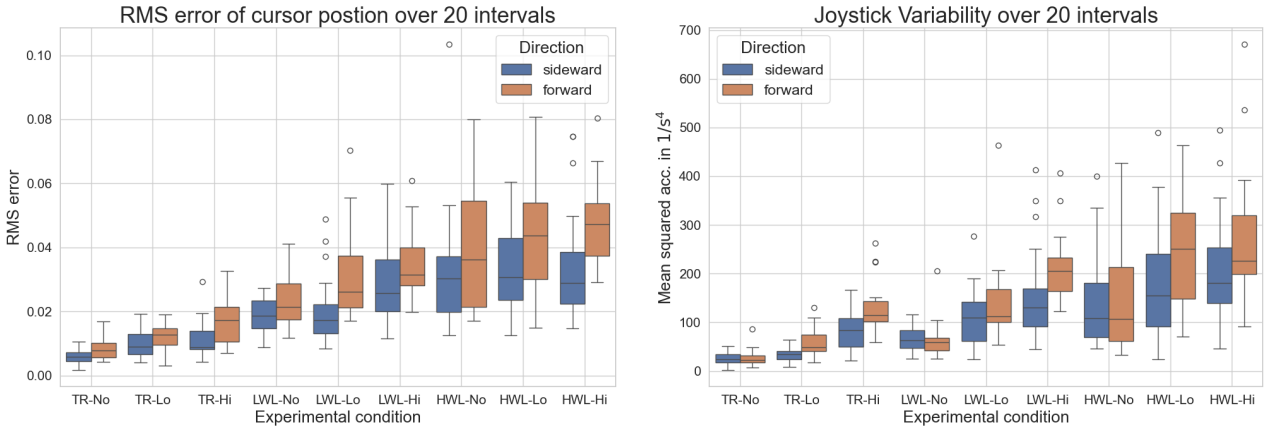



Figure 5 – Cursor sideward and forward position over time for all nine conditions of the study. Tracking errors increased, and the cursor position signal exhibited heightened variability with increased workload and turbulence.

Fig. 4 depicts the joystick input during the tracking task for the tracking-only conditions. The sinusoidal input pattern observed across all conditions results from the simulated force in MATB, which continuously displaces the cursor and therefore requires compensatory recentering by the participant. It is evident that even in the tracking-only condition without turbulence, the joystick signal is not perfectly smooth. Possible contributing factors include visual noise during target acquisition, motor command variability, and feedforward errors in estimating joystick and cursor responses. With increasing turbulence intensity, deviations from the ideal sinusoidal pattern become increasingly pronounced, indicating an influence of turbulence via BDFT on joystick input.

The plots in fig. 5 illustrate the temporal evolution of the cursor position across all nine experimental conditions. From left to right, workload increases, whereas turbulence intensity increases from top to bottom. A clear trend can be observed: tracking errors in both the forward and sideward directions increase with turbulence intensity and workload.

Comparative analysis of Fig. 5 indicates that increasing workload by one level has a stronger impact on tracking error than increasing turbulence intensity by one level. However, the resulting error patterns become more heterogeneous with increasing workload, whereas turbulence primarily increases the overall amplitude of the fluctuations in a more uniform manner.




(a) (b)

Figure 6 – (a) RMS error of cursor position for sideward and forward direction. (b) Average squared accelerations of the joystick input signal

In Fig. 6a and Fig. 6b, statistical metrics were computed over 20 intervals of the respective time series of cursor position and joystick input. The primary metric used to quantify MATB tracking performance is the root mean squared (RMS) error of the cursor position. Fig. 6a presents boxplots of the RMS error for the sideward and forward directions across all conditions. In the forward direction, a monotonic increase in RMS error is visible across both turbulence and workload conditions. As suggested by fig. 5, increasing turbulence by two levels has a slightly smaller effect than increasing workload by one level. The qualitative behaviour in the sideward direction is comparable to that in the forward direction. However, the influence of turbulence on RMS error is less pronounced than in the forward direction, as no increase is observable between some conditions.
Due to the single-subject design, statistical tests were performed on the 20 time intervals to assess the consistency of the observed patterns within the subject, rather than to infer population-level effects. First, an Kruskal-Wallis test followed by a Holm corrected Mann-Whitney-U test was performed for the RMS error. The analysis was conducted separately for the tracking-only, low-workload, and high-workload conditions to identify consistent differences between turbulence levels. Subsequently, the same analysis was performed separately for each turbulence level to investigate the effect of workload on tracking performance.

- **Impact of turbulence on tracking task performance:** Consistent influence of turbulence on RMS error were observed between the no-turbulence and high-turbulence levels for the tracking-only ($p < 0.001$) and low-workload conditions ($p < 0.05$) for all directions. In the sideward direction, a consistent difference between no- and low-turbulence was observed only in the tracking-only condition ($p < 0.05$). Differences between low and high turbulence were found only for the tracking-only condition in the forward direction and for the low-workload condition in the sideward direction ($p < 0.05$). For the high-workload conditions, no consistent differences between turbulence levels were identified.

- **Impact of workload on tracking task performance:** Consistent differences between the tracking-only and high-workload conditions were observed for all turbulence levels ($p < 0.001$). Differences between the tracking-only and low-workload conditions were also consistent for all turbulence levels ($p < 0.001$). RMS errors were consistently higher under high workload compared to low workload ($p < 0.05$), except for the sideward direction under high turbulence conditions.

Figure 6b illustrates the variability of the joystick input over 20 intervals of the time series. Variability was quantified using the mean squared acceleration of the normalized joystick position. Similar to RMS error a general trend can be observed: variability increases with both workload and turbulence intensity. In contrast to Fig. 6a, the effect of turbulence appears to be more pronounced. For both directions, variability increases by a comparable amount with increasing workload in the absence

of turbulence. Interestingly, joystick variability differs between the sideward and forward directions under turbulence conditions, indicating a direction-dependent influence of BDFT on joystick input. With increasing turbulence intensity, variability in the forward direction increases more rapidly than in the sideward direction.
Statistical analysis of joystick variability indicates an influence of both turbulence intensity and workload. However, with increasing workload or turbulence intensity, it becomes more difficult to distinguish between the individual effects. Consequently, consistency of the observed patterns for turbulence decreases under high workload conditions, and vice versa. Similar to the RMS error analysis, an Kruskal-Wallis followed by a Mann-Whitney-U test was performed.

- **Impact of turbulence on joystick variability:** For the tracking only and low workload condition consistent differences have been found in both directions between no turbulence and high turbulence ($p<0.001$). Between low and high turbulence a consistent difference was found for all except the sideward direction under low workload ($p<0.05$). Between no turbulence and low turbulence in forward direction a difference was found ($p<0.001$). In the high workload condition effects were less clear. Only in forward direction a consistent difference between no and high turbulence was found ($p<0.05$).
- **Impact of workload on joystick variability:** Statistical analysis showed for all conditions similar results for both directions. For the no turbulence condition a consistent difference between tracking only and high workload ($p<0.001$) as well as between low and high workload ($p<0.05$) was observed. In the low turbulence condition consistent differences were found between all workload levels except for the sidewards direction between low workload and high workload ($p<0.001$ between tracking only and low workload as well as between tracking only and high workload, and $p<0.05$ between low workload and high workload). In the high turbulence condition, consistent differences were found between the tracking only and low workload, as well as the tracking only and high workload condition ($p<0.001$).

Table 2 – Change of tracking task related quantities between conditions

(a) Differences in RMS cursor error

| | Δ RMS sideward [1] | Δ RMS forward [1] |
|---|---|---|
| **Turbulence** | | |
| no → Low | 0.0021 | 0.0052 |
| low → High | 0.0038 | 0.0036 |
| **Workload** | | |
| no → Low | 0.015 | 0.019 |
| low → High | 0.014 | 0.015 |

(b) Differences in mean squared accelerations of joystick input

| | Δ Var. sideward [$1/s^4$] | Δ Var. forward [$1/s^4$] |
|---|---|---|
| **Turbulence** | | |
| no → Low | 0.051 | 0.16 |
| low → High | 0.11 | 0.046 |
| **Workload** | | |
| no → Low | 0.19 | 0.23 |
| low → High | 0.17 | 0.25 |

Based on the statistical analysis, both workload and turbulence intensity appear to affect tracking performance as well as joystick input patterns. Tables 2a and 2b therefore focus on the magnitude of these effects. The tables present the average change in the corresponding quantity across all workload or turbulence levels, respectively.
Table 2a emphasizes that increasing workload by one level produces a considerably greater effect on RMS error than increasing turbulence by one level. In contrast, changes in workload and turbulence intensity have effects of comparable magnitude on joystick input variability (see Table 2b).
Figure 6b suggests a directional dependency in joystick variability with increasing turbulence intensity. To investigate this effect, an independent t-test between the RMS cursor errors in the forward and sideward directions was performed for all experimental conditions (see table 3). Within the tracking-only conditions, statistically consistent differences were identified for the low-turbulence ($p = 0.004$) and high-turbulence ($p = 0.001$) conditions, whereas no difference was observed under no turbulence. For the conditions with additional workload no consistent results have been found, possibly due to the increased scatter between the intervals. However, the p-values for the conditions with turbulence are considerably lower than without. These findings suggest that the simulated turbulence exerts a stronger influence on the forward compared to the sideward direction.

Table 3 – Comparison of joystick variability between upward and sideward deflection

| Condition | p-value |
|---|---|
| TR-No | 0.855 |
| TR-Lo | 0.004 |
| TR-Hi | 0.001 |
| LWL-No | 0.844 |
| LWL-Lo | 0.067 |
| LWL-Hi | 0.299 |
| HWL-No | 0.769 |
| HWL-Lo | 0.053 |
| HWL-Hi | 0.186 |

### 3.2 MATB-II System Monitoring and Resource Management Tasks

Resource management performance indicated lower deviations under high workload conditions compared to low workload, whereas system monitoring activity remained stable across all experimental conditions. Overall, no systematic monotonic trends were observed regarding the influence of workload or turbulence on task performance.

### 3.3 Subjective Workload

Subjective workload increased systematically with both workload and turbulence level, peaking in the high workload and high turbulence condition (see table 4). The global TLX score increased from 0.18 to 2.92 with increasing turbulence in the tracking only condition. Also, increased workload lead to higher TLX scores in the absence of turbulence, peaking in a value of 4.38 for the high workload condition. Overall, the NASA-TLX scores indicate that both intrinsic task requirements and external perturbations contribute to perceived operator strain.

Table 4 – NASA-TLX results for all experimental conditions

| Condition | Mental | Physical | Time Press. | Performance | Effort | Frustration | TLX Global |
|---|---|---|---|---|---|---|---|
| Baseline | 0.00 | 0.00 | 0.00 | 0.00 | 0.00 | 0.00 | 0.00 |
| TR-No | 0.00 | 0.13 | 0.00 | 0.28 | 0.00 | 0.64 | 0.18 |
| TR-Lo | 2.64 | 2.97 | 2.50 | 3.04 | 2.50 | 3.22 | 2.81 |
| TR-Hi | 2.94 | 2.73 | 3.01 | 3.17 | 3.17 | 2.50 | 2.92 |
| LWL-No | 1.91 | 0.79 | 2.07 | 2.85 | 1.81 | 1.39 | 1.80 |
| LWL-Lo | 3.52 | 1.75 | 3.06 | 3.11 | 3.52 | 2.18 | 2.86 |
| LWL-Hi | 5.06 | 3.39 | 3.97 | 3.34 | 3.42 | 4.64 | 3.97 |
| HWL-No | 2.96 | 1.17 | 3.66 | 7.19 | 6.29 | 5.00 | 4.38 |
| HWL-Lo | 2.94 | 2.96 | 5.62 | 4.32 | 4.96 | 5.00 | 4.30 |
| HWL-Hi | 7.49 | 5.98 | 7.29 | 5.14 | 5.00 | 4.60 | 5.92 |

### 3.4 Simulation of Biodynamic Feedthrough

Figure 7a presents the predicted RMS cursor error in the sideward (blue) and forward (green) directions using the parameter-optimized model described in section 2.5. The tracking-only condition was simulated for no-, low-, and high-turbulence intensities. The experimental results for the forward and sideward directions are shown in red and orange, respectively. Across all simulated conditions, a close agreement between simulation and experimental data can be observed.

Figures 7b and 7c compare the simulated cursor and joystick positions with the corresponding experimental data obtained from the participant. Qualitative comparison of the signals shows similar patterns in both cursor position and joystick input. The simulated joystick signal exhibits a high-frequency oscillation across all turbulence levels that is not present in the experimental data. Since this behaviour is also visible in the no-turbulence condition, it is likely an artefact of the tracking controller, rather than being caused by the pilot model. Nevertheless, the effect of simulated BDFT on




Figure 7 – (a) RMS error of cursor position. Simulation results versus Experimental data. (b) Cursor position over time for experiment and simulation in all three turbulence levels. (c) Joystick position over time for experiment and simulation in all three turbulence levels.

the task execution appears to be represented sufficiently, since the characteristic deflections of the joystick are realistically reproduced.

Table 5 – Relative error in prediction of RMS cursor error

| Turbulence | Sideward (%) | Forward (%) |
|---|---|---|
| No | -15.1 | 2.3 |
| Low | 8.3 | -0.5 |
| High | -8.3 | 6.6 |

Table 6 – Permutation test RMS sideward

| Turbulence | p-value |
|---|---|
| No | 0.644 |
| Low | 0.716 |
| High | 0.286 |

Table 7 – Permutation test RMS forward

| Turbulence | p-value |
|---|---|
| No | 0.573 |
| Low | 0.621 |
| High | 0.890 |

Table 5 presents the relative error between the predicted RMS cursor error and the experimental measurements. For all simulated conditions except the no-turbulence condition in the sideward direction, a relative error well below $10\%$ was achieved. On average, the relative error amounts to $6.9\%$.

A two-sided permutation test was performed on the RMS errors computed over 20 intervals of the experimentally collected and simulated time series to assess model-experiment consistency. No consistent differences between simulation and experimental data were identified. Tables 6 and 7 summarize the resulting p-values for the three turbulence conditions in the sideward and forward directions. Based on the qualitative comparison and statistical analysis, the model quality is assumed to be sufficient to be used to estimate the BDFT induced error in the tracking task. Using simulation of BDFT on the MATB tracking task provides a more isolated measure of the performance decrease induced by aircraft motion.

| | **BDFT induced joystick error** | |
|---|---|---|
| Turbulence | Sideward | Forward |
| No | 0.000 | 0.000 |
| Low | 0.026 | 0.044 |
| High | 0.051 | 0.078 |

Table 8 – Estimated BDFT induced error on the stick input

Table 8 presents the estimated BDFT-induced error on joystick position for the different turbulence

conditions as an example of an insightful quantity that can be derived with the BDFT model. This error is calculated using the RMS of $\delta_{ref} - \delta_{act}$. The values in the table are the increase in RMS joystick error compared to the no turbulence condition. A directional dependency, like observed in the joystick input variability can also be identified in the estimated BDFT-induced error.

## 3.5 Neurophysiological Measures

### *3.5.1 EEG and Power Spectral Density*

The analysis of EEG-derived workload indices and spectral band ratios reveals consistent modulation of cognitive load across experimental conditions involving task demand and environmental turbulence. The EEG workload index demonstrated a monotonic increase under severe turbulence conditions, indicating elevated cognitive effort associated with increased environmental complexity.

Spectral analysis was conducted using normalized EEG bandpower ratios due to instability observed in absolute bandpower magnitudes following preprocessing and aggregation. Consequently, theta/alpha, beta/alpha, and theta/beta ratios were used as primary indicators of workload and neural engagement.

Results in table 9 indicate that the theta/alpha ratio remained relatively stable across baseline and low workload conditions, ranging approximately between 2.87 and 2.90. A slight reduction in this ratio was observed under severe turbulence conditions, suggesting altered cortical engagement patterns under high environmental stress. Similarly, beta/alpha ratios remained within a narrow range ( 0.78–0.80), indicating consistent cognitive effort levels across most conditions, with marginal increases under turbulence.

The convergence of workload index and EEG spectral ratios suggests that environmental turbulence exerts a stronger influence on cognitive load than task difficulty alone. This aligns with established findings in aviation neuroscience and human factors research, where external stressors often dominate cortical activation patterns compared to controlled task manipulations.

Table 9 – Workload index and EEG band ratios across conditions

| Condition | Workload Index (%$\Delta$) | $\theta/\alpha$ Ratio | $\beta/\alpha$ Ratio | $\theta/\beta$ Ratio |
|---|---|---|---|---|
| Baseline | 0.00 | 2.88 | 0.79 | 3.64 |
| TR-No | 0.14 | 2.88 | 0.80 | 3.60 |
| LWL-No | 0.04 | 2.89 | 0.79 | 3.65 |
| HWL-No | 0.29 | 2.90 | 0.79 | 3.66 |
| TR-Lo | 0.05 | 2.87 | 0.79 | 3.60 |
| LWL-Lo | 0.26 | 2.87 | 0.79 | 3.60 |
| HWL-Lo | 0.12 | 2.89 | 0.79 | 3.64 |
| TR-Hi | 0.73 | 2.86 | 0.80 | 3.57 |
| LWL-Hi | 0.91 | 2.87 | 0.80 | 3.58 |
| HWL-Hi | 0.93 | 2.87 | 0.80 | 3.58 |

The EEG-derived workload index was evaluated across task workload conditions and environmental turbulence levels, with Baseline serving as the reference condition (mean = 3.206). Across all experimental conditions, the workload index remained within a narrow range (3.206–3.236), corresponding to a maximum relative change of approximately 0.93%. While the absolute magnitude of variation is modest, the results reveal a clear and structured modulation of workload driven primarily by environmental turbulence.

Under no turbulence conditions, workload differences attributable to task level were minimal but directionally consistent. The TrackingOnly condition exhibited a small increase (+0.14%) relative to baseline, while Low Workload and High Workload conditions showed +0.04% and +0.29% increases, respectively. Although high-workload tasks produced slightly elevated values compared to low-workload tasks, the effect size remained small, indicating limited sensitivity of the EEG workload index to task difficulty in the absence of environmental perturbation. These findings suggest that, under stable conditions, cognitive demand associated with task manipulation alone induces only marginal changes in workload indicators.

Table 10 – Workload index changes across experimental conditions

| Condition | Workload Index | Δ Workload | % Change |
|---|---|---|---|
| Baseline | 3.206 | 0.000 | 0.00 |
| TR-No | 3.211 | 0.004 | 0.14 |
| LWL-No | 3.207 | 0.001 | 0.04 |
| HWL-No | 3.215 | 0.009 | 0.29 |
| TR-Lo | 3.208 | 0.002 | 0.05 |
| LWL-Lo | 3.214 | 0.008 | 0.26 |
| HWL-Lo | 3.210 | 0.004 | 0.12 |
| TR-Hi | 3.230 | 0.024 | 0.73 |
| LWL-Hi | 3.235 | 0.029 | 0.91 |
| HWL-Hi | 3.236 | 0.030 | 0.93 |

With the introduction of light turbulence, a modest increase in workload variability is observed (see table 10). Relative changes ranged between +0.05% and +0.26% across conditions; however, no consistent monotonic relationship between low and high workload tasks is evident. The attenuation of task-level differentiation suggests that even moderate environmental instability begins to interfere with the separability of task-induced cognitive states. In this regime, workload appears to reflect a combined influence of task demands and environmental uncertainty, without a dominant factor.
A pronounced shift in workload dynamics is observed under severe turbulence. All conditions exhibit a clear and consistent elevation in EEG-derived workload, ranging from +0.73% to +0.93% relative to baseline. Importantly, task-level differences collapse under this condition, with low workload (0.91%) and high workload (0.93%) converging to nearly identical values. This convergence indicates a saturation effect, where elevated environmental demand dominates cognitive resource allocation and suppresses discriminability between task difficulty levels. The results strongly suggest that severe turbulence imposes a dominant cognitive load that overrides task-specific workload modulation.
Overall, the findings demonstrate that environmental turbulence is the primary determinant of EEG-based workload variation in this experimental paradigm. While task workload contributes marginally under low-stress conditions, its influence diminishes progressively as turbulence increases. The observed interaction indicates that high environmental demand not only elevates workload but also reduces the sensitivity of EEG measures to task-level differences, leading to convergence across workload conditions. These results highlight the importance of accounting for environmental stressors when interpreting EEG-derived workload metrics in operational settings.

### *3.5.2 Cardio-Respiratory Dynamics*

Cardio-respiratory measurements were analyzed to investigate the sensitivity of autonomic indicators to workload and turbulence exposure. Given that this study was conducted as a proof-of-concept pilot experiment involving a single participant, the results should be interpreted as exploratory observations rather than evidence of population-level physiological responses.

Table 11 – Cardio Respiratory Features Across Selected Experimental Conditions

| Feature | Baseline | HWL-No | LWL-No | TR-Hi | LWL-Hi | HWL-Hi |
|---|---|---|---|---|---|---|
| Heart Rate (bpm) | 97.47 | 98.58 | 98.03 | 72.84 | 52.17 | 44.01 |
| Hexoskin HR (Raw) | 61.95 | 73.07 | 71.41 | 72.10 | 73.33 | 76.94 |
| HR Fusion | 62.22 | 73.01 | 71.52 | 72.08 | 73.09 | 77.28 |
| HR BLE | 61.97 | 73.06 | 71.41 | 72.12 | 73.34 | 76.97 |
| HRV ($ms^2$) | 247.19 | 207.87 | 199.35 | 582.54 | 1022.63 | 957.76 |
| Respiration Rate | 12.53 | 18.01 | 17.86 | 15.07 | 15.04 | 14.02 |
| Respiration Fusion | 12.50 | 18.04 | 17.89 | 15.01 | 15.07 | 14.06 |

The cardiovascular measurements revealed a clear distinction between the derived heart rate feature and the directly measured heart rate estimates obtained from the wearable sensing systems (see

table 11). The aggregated heart rate feature decreased from 97.47 bpm at baseline to 52.17 bpm and 44.01 bpm during the LWL-Hi and HWL-Hi conditions, respectively. However, this trend was not observed in the Hexoskin Raw, HR Fusion, or HR BLE measurements. Instead, all three heart rate estimates exhibited relatively consistent increases from baseline values of approximately 62 bpm to values between 73 and 77 bpm under severe turbulence conditions.

The disagreement between the derived heart rate feature and the three independent heart rate measurements suggests that the pronounced decrease observed in the aggregated feature is unlikely to represent a true physiological response. A more plausible explanation is the presence of motion-induced artifacts caused by increased relative movement between the participant and the smart garment during severe turbulence. Such movement can alter sensor-to-skin contact and introduce friction-related disturbances that propagate into derived cardiovascular metrics. Consequently, the decrease in the aggregated heart rate feature should be interpreted with caution and not as evidence of autonomic suppression.

Heart rate variability (HRV) exhibited the largest relative changes across all cardiovascular features. HRV increased from 247.19 $ms^2$ during baseline to 582.54 $ms^2$ during the TrackingOnly-HighTurb condition and exceeded 950 $ms^2$ during both workload-related high-turbulence conditions. These observations indicate that HRV-derived metrics are highly sensitive to turbulence exposure. However, because HRV estimation depends on accurate beat detection, the potential influence of motion-induced artifacts cannot be excluded and warrants further investigation.

Respiratory measures displayed comparatively moderate variation across conditions. Respiration rate increased from approximately 12.5 breaths/min during baseline to approximately 18 breaths/min under workload-only conditions and subsequently decreased to approximately 14–15 breaths/min during severe turbulence exposure. The close agreement between the direct respiration measurements and the fusion-based estimates across all conditions suggests that respiratory sensing remained comparatively robust despite increased simulator motion.

Overall, the results indicate that turbulence exposure influences both cardiovascular and respiratory signal characteristics while simultaneously introducing measurement challenges associated with wearable sensing in dynamic environments. These findings highlight the importance of incorporating signal-quality assessment and artifact-mitigation techniques when using physiological measurements for operator-state estimation in turbulence-affected flight scenarios.

### *3.5.3 Statistics of Neurophysiological Features*

To evaluate the sensitivity of the extracted neurophysiological and physiological features to workload and turbulence conditions, a Kruskal–Wallis analysis was performed across all experimental conditions. Since the present study involved a single participant, the resulting statistical tests should be interpreted as measures of within-subject condition-dependent variation rather than evidence of population-level significance.

The 43 exhibited statistically detectable differences across conditions ($p < 0.05$), indicating that a large proportion of the recorded measurements were sensitive to changes in workload, turbulence exposure, or their interaction.

Cardiovascular features demonstrated some of the strongest condition-dependent effects. Heart rate measurements derived from the Hexoskin system and fusion-based processing pipeline showed highly significant variation across conditions (e.g., HeartRateFusionFeature: $H = 3031.43$, $p < 0.001$). Consistent with the observations in Table 11, these measurements generally increased from baseline during workload and turbulence exposure, reaching their highest values under severe turbulence conditions. This pattern suggests that cardiovascular metrics are sensitive to combined cognitive and biodynamic stressors.

Heart rate variability measures also exhibited significant condition-dependent changes. In contrast to the direct heart rate estimates, HRV increased substantially during severe turbulence conditions. While this finding may reflect increased physiological variability associated with motion exposure, the potential contribution of turbulence-induced sensing artifacts must also be considered, particularly given the wearable nature of the measurement system.

Respiratory features showed significant variation across conditions, with respiration rate increasing during workload-only conditions and remaining elevated relative to baseline throughout the turbulence

scenarios. The consistency between direct and fusion-based respiration estimates suggests that respiratory measurements were less susceptible to turbulence-induced artifacts than cardiovascular measures.

Acceleration-derived biodynamic features exhibited strong sensitivity to turbulence exposure (e.g., sagittalAccelerationInG: $H = 1719.87$, $p < 0.001$), reflecting the increased physical motion experienced by the participant during simulator movement. These findings are consistent with the expected influence of turbulence on body dynamics and support the inclusion of biodynamic measurements within adaptive control-allocation frameworks.

Taken together, the results suggest that turbulence exposure produced more pronounced changes across the physiological and biodynamic feature set than workload manipulation alone. While these observations are limited to a single participant and therefore cannot be generalized, they provide preliminary evidence that both neurophysiological and biodynamic signals are sensitive to environmental perturbations and may contain useful information for future adaptive control-allocation approaches.

## 4. Discussion towards Fusion of Body Dynamics and Neurophysiological Sensing

The results of the tracking task, BDFT modelling, and neurophysiological measurements provide preliminary support for both hypotheses introduced in Section 2.1. A key observation is that the two modalities characterize different aspects of pilot state. Body-dynamics features primarily quantify the external effects of turbulence on task execution and control behaviour, whereas neurophysiological measures provide information related to cognitive workload, autonomic regulation, and physiological adaptation. Neither modality alone therefore provides a complete representation of operator state during dynamic flight conditions.

From the perspective of the STAR framework, these findings suggest that body dynamics and neurophysiological sensing should be viewed as complementary rather than competing sources of information. Body-dynamics measures can provide direct information regarding turbulence-induced control limitations and BDFT effects, while neurophysiological signals provide insight into the pilot's cognitive and physiological response to those disturbances. The combination of both modalities may therefore enable a more comprehensive estimate of pilot state than either source alone.

Such a multimodal approach could be particularly valuable for adaptive control allocation. A pilot may experience performance degradation primarily due to physical disturbances, while cognitive workload remains relatively unchanged. Conversely, elevated cognitive demand may emerge before measurable degradation in control performance becomes apparent. By jointly considering body-dynamics and neurophysiological information, future adaptive systems may be better able to distinguish between these scenarios and allocate authority accordingly.

The following paragraphs provide a more technical discussion of the results from section 3. in more detail.

### 4.1 Effects of Cockpit Accelerations on Pilot Performance Capabilities

The results in Section 3.1 indicate that the *Performance Difference Hypothesis* holds for the tested subject: RMS tracking error increased consistently between no- and high-turbulence conditions in both tracking-only and low-workload scenarios. Joystick variability also increased with turbulence, particularly in the forward direction. These results indicate that acceleration perturbations affect pilot related fine motor tasks such as the MATB tracking task.

Workload and turbulence affect performance in different proportions. Workload produces a stronger increase in RMS error across conditions, whereas turbulence has a weaker effect on overall error but a stronger effect on joystick variability. This suggests that the task is affected by another mechanism that needs to be distinguished from mental workload and that adds up to the resulting task performance: biodynamic feedthrough.

Directional differences in joystick input variability and the estimated BDFT-induced error in low- and high-turbulence condition further support this interpretation. In contrast to the conditions with no turbulence where no directional difference can be observed, the forward direction was consistently more affected by the turbulence than the sideward direction, aligning with the applied acceleration patterns, which exert a higher power in forward than in sideward direction.

The magnitude of the observed BDFT effects is likely underestimated due to the limited acceleration capabilities of a motion simulator. Thus, results likely represent a lower bound compared to operational flight conditions or higher G-loads.
For the systems monitoring and resource management tasks of MATB these findings do not allow for clear conclusions about the effects of workload and turbulence due to the study's limitation of a single subject. Additionally, the ascending order of conditions likely introduced practice effects, which may have artificially improved performance during high turbulence trials.

## 4.2 Implications for Neurophysiological Pilot State Estimation

The findings support the *Neurophysiological Correlation Hypothesis*. Neurophysiological signals such as EEG and heart rate showed sensitivity to both workload and the motion environment. Subjective workload ratings also increased with turbulence, supporting the observed behavior. However, statistical conclusions are limited by the single-subject design.
EEG signals are assumed to be largely robust to motion artefacts while still showing differences between turbulence conditions, suggesting sensitivity to acceleration-related state changes beyond pure measurement noise.
In contrast, heart rate and related cardiovascular measures showed inconsistent effects across turbulence levels, likely due to stronger contamination by motion artefacts (e.g. impaired electrical connection between the sensor and the skin). This limits their reliability for direct mental state estimation in dynamic environments.
These results highlight the need to account for motion-induced effects when interpreting physiological signals for adaptive systems such as the STAR control allocation framework, as otherwise acceleration effects may be misinterpreted as workload changes.

## 4.3 Potential of BDFT-Based Features for Adaptive Filtering and Performance Estimation

The observed influence of turbulence on both performance and physiological measurements suggests that BDFT-related measures could help separate workload- and acceleration-induced effects in neurophysiological signals, enabling more robust adaptive filtering and pilot-state estimation.
Using raw acceleration measurements as input would be a first step to distinguish between both effects. However, pilot response highly depends on posture, device characteristics, motor control and task constraints. In contrast to cockpit acceleration alone, BDFT related features capture task-relevant effects of motion on control behaviour and are therefore more informative for predicting performance degradation.
The proposed BDFT model transforms acceleration into task-relevant performance effects by explicitly linking human body dynamics with the MATB tracking task. This provides a direct mapping from motion to control behaviour.
Because the model is physics-based and incorporates biomechanical, device and task characteristics, it is expected to generalize better to different manoeuvres and higher accelerations than purely data-driven approaches. Simulation results support the validity of the derived model, showing good agreement with experimental tracking errors.

## 4.4 Limitations and Future Work

Statistically distinguishable patterns were assessed on time-interval segments of a single subject. While this demonstrates within-subject consistency, the results should be interpreted as exploratory and require validation with a larger cohort.
The BDFT model is task-specific and validated only for the MATB-II tracking task. Other interaction modalities (e.g., typing or touchscreen input) likely require separate modelling.
Finally, the limited motion capabilities of the simulator likely led to an underestimation of BDFT effects.
Overall, the results highlight the potential of integrating BDFT modelling into neurophysiological pilot monitoring systems. Explicit modelling of the interaction between acceleration, body dynamics, and task execution may enable more robust and context-aware pilot state estimation.

## 5. Conclusion

This study investigated the integration of neurophysiological signals and human body dynamics with the ultimate goal of enhancing adaptive control allocation within the STAR framework. The findings indicate that aircraft motion is a relevant factor for pilot state and performance estimation, due to biodynamic feedthrough (BDFT), and the modulation of neurophysiological signals by turbulence, supported by increased subjective workload ratings. A critical observation is that workload and turbulence are not easily distinguished using neurophysiological signals and joystick input patterns alone. Therefore, estimating the BDFT-induced task error by simulation could provide a powerful quantity to distinguish between these stressors. Furthermore, this approach covers task-relevant properties, constituting an important step from pure state estimation to performance prediction.

The added value of this work lies in providing a more realistic environment for the investigation of mental states and performance prediction on the way towards adaptive control allocation. The results imply that in a moving environment, there are at least two distinct sources of performance degradation: workload and aircraft motion. Not accounting for the consequences of motion could lead to wrong estimations of pilot state and task performance. However, as a part of adaptive control systems such as STAR, a reliable pilot state estimation is crucial. Consequently, the adaptive interpretation of neurophysiological signals using the BDFT-induced performance degradation seems relevant to be explicitly accounted for in future systems.

Moving forward, attention in mental state modeling research of pilots should shift towards more realistic setups to facilitate application. As this work serves as a first indication, studies with a larger number of subjects need to be conducted to obtain more reliable results and quantify the observed effects.

## 6. Contact Author Email Address

tobias.treichl@dlr.de
tanya.paul@thalesgroup.com

## 7. Copyright Statement

The authors confirm that they, and/or their company or organization, hold copyright on all of the original material included in this paper. The authors also confirm that they have obtained permission, from the copyright holder of any third party material included in this paper, to publish it as part of their paper. The authors confirm that they give permission, or have obtained permission from the copyright holder of this paper, for the publication and distribution of this paper as part of the ICAS proceedings or as individual off-prints from the proceedings.

## References

[1] T. S. Paul, et al. “Public Safety Personnel Readiness Prediction: A Hybrid Model of Neurophysiological and Psychometric Data,” in *Adaptive Instructional Systems (HCII 2025)*, Lecture Notes in Computer Science, vol. 15812, R. A. Sottilare and J. Schwarz, Eds. Springer, Cham, 2025, doi: 10.1007/978-3-031-92967-0_16.

[2] T. S. Paul, D. Lafond, and P.-Y. Benzakine. AI-driven collaboration mode selection for manned-unmanned teaming in future combat air systems, in 2025 *International Conference on Military Communication and Information Systems (ICMCIS)*, Oerias, Portugal: IEEE, May 2025, pp. 1–10.

[3] T. S. Paul and D. Lafond. Meaningful human control in multi-agent systems, *NATO Human Factors and Medicine Panel*

[4] G. Singh, C. P. C. Chanel, and R. N. Roy. Mental workload estimation based on physiological features for pilot-UAV teaming applications, *Front. Hum. Neurosci.*, vol. 15, p. 692878, Aug. 2021.

[5] C. Neubauer et al. Multimodal physiological and behavioral measures to estimate human states and decisions for improved human autonomy teaming, 2020.

[6] B. Raufi and L. Longo, “An Evaluation of the EEG Alpha-to-Theta and Theta-to-Alpha Band Ratios as Indexes of Mental Workload,” *Frontiers in Neuroinformatics*, vol. 16, May 2022, doi: 10.3389/fninf.2022.861967.

[7] I. Albuquerque et al. WAUC: A multi-modal database for mental workload assessment under physical activity, *Front. Neurosci.*, vol. 14, p. 549524, Dec. 2020.

[8] T. Bellmann, A. Seefried, and B. Thiele. The DLR robots library – Using replaceable packages to simulate various serial robots," *Asian Modelica Conference 2020*, pp. 153–161.

[9] T. Treichl., Simulation of the human arm dynamics and motor control in unstable environments: A comparison with experimental data, *IEEE International Conference on Systems, Man, and Cybernetics (SMC)*, Honolulu, Oahu, HI, USA: IEEE, Oct. 2023.

[10] T. Treichl. Using the internal model hypothesis to model human motor control in multi-domain simulations, *IEEE International Conference on Systems, Man, and Cybernetics (SMC)*, Vienna, Austria: IEEE, Oct. 2025.

[11] T. Treichl, D. Milz, T. Bellmann, and A. Seefried. Multi-domain simulation of human mechanics for dynamic analysis, *IEEE International Conference on Systems, Man, and Cybernetics (SMC)*, Prague, Czech Republic: IEEE, Oct. 2022.

[12] J. Cegarra, B. Valéry, E. Avril, C. Calmettes, and J. Navarro. OpenMATB: A multi-attribute task battery promoting task customization, software extensibility and experiment replicability, *Behav Res*, vol. 52, no. 5, pp. 1980–1990.

[13] S. V. Löhlein. Development of a test scenario to Assess kinetosis risk in military flight training, *22nd International Symposium on Aviation Psychology*.

[14] T. Bellmann, M. Otter, and G. Hirzinger. The DLR robot motion simulator part II: optimization based path-planning, *IEEE International Conference on Robotics and Automation*, Shanghai, China: IEEE, May 2011.

[15] P. Antonenko, F. Paas, R. Grabner, and T. van Gog, "Using electroencephalography to measure cognitive load," *Educational Psychology Review*, vol. 22, pp. 425–438, 2010.

[16] S. G. Hart and L. E. Staveland, "Development of NASA-TLX (Task Load Index): Results of empirical and theoretical research," in *Advances in Psychology*, vol. 52, 1988, pp. 139–183.

[17] T. M. Ichwanul Hakim and O. Arifianto. Implementation of Dryden continuous turbulence model into Simulink for LSA-02 flight test simulation, *J. Phys.: Conf. Ser*, Apr. 2018

[18] Y. Santiago-Espada, R. R. Myer, K. A. Latorella, and J. R. Comstock. The multi-attribute task battery II (MATB-II) software for human performance and workload research: A user's guide

[19] S. G. Hart and L. E. Staveland. Development of NASA-TLX (Task Load Index): Results of Empirical and Theoretical Research, *Advances in Psychology*, vol. 52, Elsevier, 1988

[20] R. S. Kennedy, N. E. Lane, K. S. Berbaum, and M. G. Lilienthal. Simulator Sickness Questionnaire: An Enhanced Method for Quantifying Simulator Sickness, *The International Journal of Aviation Psychology*, vol. 3, no. 3, pp. 203–220, Jul. 1993.

[21] T. Blochwitz et al. The Functional Mockup Interface for Tool independent Exchange of Simulation Models, *8th International Modelica Conference*, Technical Univeristy, Dresden, Germany, Jun. 2011, pp. 105–114.